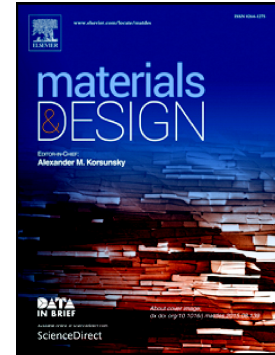


Accepted Manuscript

3D-printed biodegradable gyroid scaffolds for tissue engineering applications

Loïc Germain, Carlos A. Fuentes, Aart W. van Vuure, Anne des Rieux, Christine Dupont-Gillain



PII: S0264-1275(18)30307-1
DOI: doi:[10.1016/j.matdes.2018.04.037](https://doi.org/10.1016/j.matdes.2018.04.037)
Reference: JMADE 3850
To appear in: *Materials & Design*
Received date: 10 November 2017
Revised date: 12 April 2018
Accepted date: 13 April 2018

Please cite this article as: Loïc Germain, Carlos A. Fuentes, Aart W. van Vuure, Anne des Rieux, Christine Dupont-Gillain, 3D-printed biodegradable gyroid scaffolds for tissue engineering applications. The address for the corresponding author was captured as affiliation for all authors. Please check if appropriate. Jmade(2017), doi:[10.1016/j.matdes.2018.04.037](https://doi.org/10.1016/j.matdes.2018.04.037)

This is a PDF file of an unedited manuscript that has been accepted for publication. As a service to our customers we are providing this early version of the manuscript. The manuscript will undergo copyediting, typesetting, and review of the resulting proof before it is published in its final form. Please note that during the production process errors may be discovered which could affect the content, and all legal disclaimers that apply to the journal pertain.

3D-printed biodegradable gyroid scaffolds for tissue engineering applications

Loïc Germain^{a,b}, Carlos A. Fuentes^c, Aart W. van Vuure^c, Anne des Rieux^{a,b,*}, Christine Dupont-Gillain^{b,*}

^a *Université catholique de Louvain, Louvain Drug Research Institute, Advanced Drug Delivery and Biomaterials, Avenue E. Mounier 73, 1200 Bruxelles, Belgium*

^b *Université catholique de Louvain, Institute of Condensed Matter and Nanosciences, Place L. Pasteur 1 (L4.01.10), 1348 Louvain-la-Neuve, Belgium*

^c *KU Leuven, Department of Materials Engineering, 3001 Leuven, Belgium*

**Corresponding authors*

Abstract

Fused deposition modeling (FDM), a low-cost and easy-to-use additive manufacturing technique, was used to produce poly(lactic acid) (PLA) gyroid scaffolds. Such morphology was selected for its spring shape, high porosity leading to good nutrient and waste diffusion, and favorable mechanical properties. Printing parameters were optimized and the need of a support material to improve printing was evidenced. The gyroid was compared to the common strut-based structure. Scaffold porosity was measured by micro-CT, and mechanical properties were determined by compression tests, taking into account the effect of geometry, printing resolution, and PLA crystallinity. The impact of scaffold geometry and crystallinity on its degradation was studied *in vitro*. Porosity of the gyroid structure was 71%, as expected from the printing model. The compression tests showed an isotropic behavior for the gyroid, in contrast with the strut-based scaffold. Upon aging in physiological conditions, gyroid scaffolds retained their integrity during 64 weeks, while control scaffolds lost struts starting from week 33, in a way that depended on crystallinity and printing resolution. Based on these results, the gyroid design is proposed as a suitable mesh architecture for tissue engineering scaffolds that can be elaborated using FDM techniques, to produce low-cost and personalized implants.

Keywords

Fused Deposition Modeling; poly(lactic acid); gyroid; scaffold

1. Introduction

Tissue engineering is an interdisciplinary field linking engineering and biology in order to recover, maintain or improve the function of a tissue or organ [1]. It focuses on three main components: cells, biomaterials and bioactive factors, that are combined to mimic the physical and chemical structure of the body [2]. These components are implanted or injected to stimulate the regeneration of a damaged tissue. Cells, usually stem cells, proliferate, differentiate and form the new tissue or, at least, improve the recovery of the lesion, notably owing to their unique immunomodulatory properties [3-5]. The biomaterial will generally be processed as a scaffold, to which bioactive compounds can be added, with a view to carry cells and guide their behavior [6, 7].

The physical properties of the scaffold are of utmost importance. The mechanical properties have to fit with the ones of the implantation site. For instance, a too soft scaffold could lose its primary shape due to compression by native tissues [8], as is the case for musculoskeletal implantations. For applications such as nasal implants, flexibility is however needed to avoid complications such as infection or extrusion [9]. The scaffold design can also impact cell attachment, proliferation, migration and differentiation [10, 11]. One important parameter influencing these cell behaviors is porosity. Indeed, pore size and interconnectivity determine communication among cells as well as nutrient, gas and waste diffusion [6, 11]. Too small pores and a lack of interconnectivity could lead to cell necrosis [8].

Scaffolds meeting these requirements can be produced with a range of different techniques such as salt leaching, gas foaming, fiber bonding, solvent casting, melt molding, phase separation, freeze drying, photolithography and electrospinning [6, 8]. Besides, Solid Freeform Fabrication (SFF) methods, also known as additive manufacturing techniques, and popularized under the name of 3D printing methods, are easier to implement to reach designs with controlled dimensions, complex shapes and high porosity. This is ensured by the layer-by-layer construction process which relies on computer-aided design/computer-aided manufacturing (CAD/CAM) systems. SFF methods do not require the use

of a mold, and models can be directly generated from computerized tomography, laser scanning or magnetic resonance imaging data, allowing the production of personalized implants [12]. Moreover, complex shapes that could not be obtained with molding can be produced based on layer-by-layer construction.

Recent research in the field of additive manufacturing for tissue engineering mainly focuses on three directions: (i) 3D bioprinting, (ii) 3D printing of polymers, and (iii) 3D printing of ceramics. The use of 3D (bio)printing concepts is sometimes confusing in the literature. 3D bioprinting refers to the production of cell-loaded scaffolds, meaning that cells are printed at the same time as the scaffold [13]. Ho and Hsu (2018) proposed a synthetic thermo-responsive waterborne polyurethane gel as bioink. Using an extrusion-based 3D printer, they demonstrated that human fibroblasts co-printed with FoxD3 plasmids in this hydrogel could be reprogrammed and differentiated into a neural-like construct [14]. Beside synthetic bioinks, natural bioinks can also be used. Di Giuseppe et al. (2018) used an alginate-gelatin mixed hydrogel. Blends were prepared by varying individual constituent concentrations and were tested for printability and printing accuracy, compressive behavior, and viability of encapsulated mesenchymal stem cells [15]. 3D printing refers to the production of inert or bioactive scaffolds. Cells can be added to such scaffolds in a second step [13]. Two main classes of materials are used for 3D printing: polymers and ceramics. The most common polymers used in additive manufacturing for tissue engineering are polylactides, poly(ϵ -caprolactone), and poly(propylene fumarate), which are selected for their mechanical stability, cytocompatibility and resorbability [13, 16]. However, most of these polymers possess a limited bioactivity. Some studies aim at modifying the scaffold surface by deposition of molecules or proteins. Teixeira et al. (2018) used polydopamine to coat PLA scaffolds and showed an improved immobilization of collagen I at the surface, increasing the scaffold osteoinductivity [17]. Ceramics such as calcium phosphate or magnesium phosphate are promising biomaterials for bone tissue regeneration [13]. Researchers are focusing on the effect of pore architecture on differentiation [18] and on the addition of dopants such as manganese [19] or of indene compounds [20] to promote bone and cartilage regeneration.

Hybrid scaffolds, which combine two features of the systems presented above, i.e. cell-loaded hydrogels, 3D printed polymers, and 3D printed ceramics, are also proposed. The addition of β -tricalciumphosphate in a copolymer hydrogel improved the physicochemical properties of the scaffold and stimulated human bone marrow stem cells proliferation and differentiation [21]. Dome-shaped tissue constructs were proposed combining PCL printing and decellularized adipose tissue matrix bioprinting. Human adipose derived mesenchymal stem cells were encapsulated and printed without any deleterious effect. Printing rather increased adipogenic genes expression [22]. Hydroxyapatite and poly(propylene fumarate) were used as coating on a PCL scaffold printed with the fused deposition modeling technique. This coating enhanced the compressive modulus, cell adhesion, and proliferation rate [23].

Most SFF techniques are unfortunately expensive. Fused Deposition Modeling (FDM) is however a low cost and easy-to-use SFF method [10]. This nozzle-based technique is based on the layer-by-layer deposition of thermoplastic polymers in a semi-liquid state along an extrusion path. It can be applied to a large variety of materials, and allows the production of patient-personalized scaffolds with a precise control of the geometry, with a typical resolution of $0.4 \times 0.4 \times 0.1 \text{ mm}^3$ [10, 24, 25].

Polymers, owing to their versatile mechanical properties and their ease of processing, have been extensively used as biomaterials in the tissue engineering field [10]. They have to fulfill several conditions in order to be used as scaffolds for this application. Among others, a suitable degradation rate, mechanical properties close to the native tissue and absence of cytotoxicity are required [9]. Poly(lactic acid) (PLA) fulfills these requirements and has also been approved by the Food and Drug Administration (FDA) as a material for several biomedical applications. Even though PLA has already been employed extensively for 3D scaffolding, the use of this biodegradable polymer has been scarcely reported for nozzle-based deposition methods [24, 25]. PLA mechanical resistance and degradation rate are influenced by its crystallinity. Crystallites present in semi-crystalline PLA are zones of high

polymer density that reinforce the material, because of a much slower degradation compared to amorphous regions [26, 27]. Therefore, scaffold mechanical properties and degradation rate could be tuned by controlling PLA crystallinity.

Nowadays, the production of scaffolds using nozzle-based systems usually consists in stacking struts of the selected material on top of each other to reach a final 3D object [6, 8, 10, 28, 29]. Many parameters related to these struts and the resulting mesh can be varied such as strut diameter, space between them and orientation from one layer to another. However, more complex mesh designs are of great interest, especially in the field of tissue engineering. The gyroid morphology (Figure 1a) is a mesh composed of units made of quadruple junction points [30]. The branches have a curved shape and link other nodes throughout the structure. This kind of mesh provides interesting features for tissue scaffolding such as mechanical energy absorption and robustness, as well as good nutrient and waste diffusion owing to the high porosity and the minimal surface area [31, 32]. Gyroids for bone implantation were already printed in titanium or stainless steel by Electron Beam Melting (EBM) or Selective Laser Melting (SLM), two SFF methods [31, 33, 34]. However, these materials are heavy, non-degradable, and not suitable for all applications. Moreover, these SFF techniques are expensive. Digital Light Printing, a photocrosslinking-based method, has also been used with success to produce gyroids in poly-(propylene fumarate) for biomedical applications [16, 35]. Gaining approval and reaching the clinics by producing photopolymerizable resins containing nontoxic photoinitiators, solvents and other additives remains however challenging. In contrast, FDM is low cost, easy to implement and allows the use of several available medical grade thermoplastics, which could notably be biodegradable or not depending on the requirements. FDM has not been much considered for tissue engineering applications yet, probably because of its poor resolution compared to other additive manufacturing techniques. It has, to our knowledge, not yet been used for small and complex PLA model construction in the field of tissue engineering.

The aim of this work is to optimize the printing parameters of a PLA-based complex object at a scale close to the resolution limit of fused deposition modeling. The gyroid design will be used as a mesh for the 3D printing of scaffolds in reason of its remarkable properties, including large pore size, high interconnectivity, high porous volume and isotropy. The effect of mesh design, polymer crystallinity, and printing layer resolution on mechanical properties and degradation rate will also be assessed.

2. Materials and methods

2.1. 3D models

The gyroid 3D model was downloaded from the 3DVIA website (Internet reference 1) and modified with an open source software (Blender V2.69.0, Blender Foundation, The Netherlands). The whole structure was made four times thicker to enable its printing with a common fused deposition modelling apparatus. Control models were also designed to produce scaffolds made of struts stacked on top of each other (Figure 1b), as often done in the literature related to 3D-printed scaffolds [6, 8, 10, 28, 29]. These models were drawn with the 123D Design software (Autodesk, V1.6) in order to have similar strut diameter and similar porous fraction as with the gyroid model.

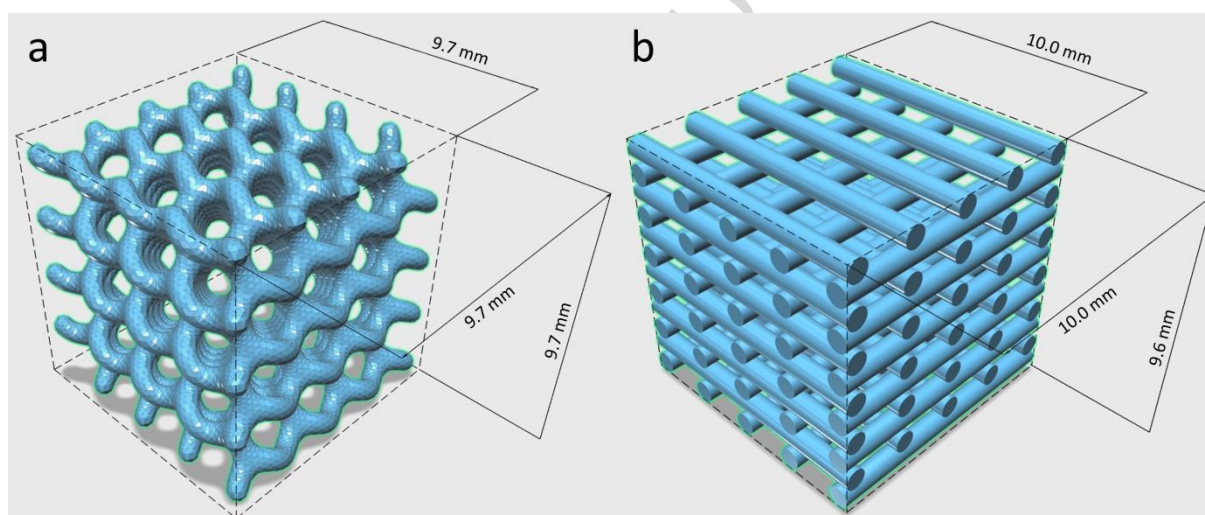


Figure 1: Gyroid 3D model (a) and control structure (strut-based scaffold) (b).

2.2. Materials and printing conditions

Polymers were printed by fused deposition modelling with a Makerbot Replicator 2X 3D printer (Makerbot, Germany) equipped with a dual extruder. Scaffolds were printed in poly(lactic acid) (PLA) (Makerbot, Germany), and High Impact polystyrene (HIPS) (Makerbot, Germany) was used as support material for printing optimization. Supports are polymer parts printed simultaneously with the structure, which carry PLA layers not supported by a layer already present underneath and would thus

be deposited on void; the support material is then removed after printing. PLA blends from Makerbot are made from pellets of NatureWorks polylactide resin 4043D (NatureWorks LLC, USA). Number-averaged molar mass (M_n) and dispersity (\mathcal{D}) values were previously determined with gel permeation chromatography using light scattering and were 57.0 kg/mol and 2.43, respectively [36]. Before printing, PLA was dried overnight at 80°C, resulting in a change of its crystallinity (see more details in sections 2.6. and 3.5.). HIPS was removed after printing by dissolution in (R)- α -Limonene (VWR, USA). Then, the use of water-soluble poly(vinyl alcohol) (PVA) (Formfutura, the Netherlands) as a support material was evaluated to avoid the immersion of the scaffold in an organic solvent, with a view to better fit the requirements for clinical use.

Once modifications were made (see 2.1), the 3D model was imported in the MakerWare software (V. 2.4.1.24) and was duplicated to enable the printing of nine objects in parallel. Custom parameters were applied to program these structures with a set of printer path instructions. For all samples, PLA was printed with a concentric pattern, and the infill density, representing the fraction of void filled with polymer inside the pillars, was set to 1. Gyroid samples (Figure 1A) were printed with a Z resolution of 100 μm and with a nozzle diameter of 400 μm . Temperatures applied for the printing of PLA, HIPS and PVA were 220°C, 250°C and 230°C, respectively. The support was printed 0.4 mm away from the structure, and its density, defined as the fraction of void filled with supporting polymer, was set to 0.5. Purge walls were printed at the sides of the printed structures to get rid of overheated polymer and to sweep the nozzles. After printing, the supporting polymer (HIPS or PVA) was dissolved in limonene or water, respectively, in 3 baths of 8 h each. The need of a supporting material was further investigated. Supported and non-supported gyroid structures were compared. For samples without support, the set of printer path instructions was exactly the same as for the one with PVA support, but no filament was loaded into the second head of the printer.

Control samples (Figure 1B) were printed without support and the flow rate through the extrusion head was optimized to get the same void fraction as for the gyroid samples. These controls were

printed with two different Z resolutions: 100 μm and 400 μm (named control 100 μm and control 400 μm , respectively, hereafter), in order to analyze the effects of the printing resolution.

2.3. μCT scan

HIPS-supported PLA scaffolds, treated with limonene to remove HIPS, were 3D imaged using a Phoenix NanoTom X-ray computed tomography equipment (General Electric Company, Fairfield, USA). This allowed the complex 3D scaffold structure to be imaged without destructive effects. The applied voltage and current were 40kV and 620 μA respectively, with a molybdenum target. The exposure time was 500 ms and a frame averaging of 3 and image skip of 1 were applied. The obtained voxel size was 6.1 μm^3 . The stack of scan images was then thresholded with CTBox software (Bruker microCT, Kontich, Belgium) to differentiate the polymer from the pores. The porous fraction was determined with the ImageJ 1.47v software (Wayne Rasband, National Institutes of Health, USA) [37]. Images were imported, cropped at the edges of the sample, thresholded into a binary stack and analyzed with the Voxel Counter plugin in ImageJ. Taking into account the distance between two images from the stack, the program evaluates the presence or absence of polymer voxel by voxel and sums up the information into a volume fraction.

2.4. Porous volume measurement

Gyroid structure porous fraction (including both accessible and possibly occluded porosity) was measured experimentally on samples printed with a PVA support that was further eliminated with water. Mass and dimensions (width, W, length, L, and height, H of the imaginary cube containing the structure) of gyroid and control structures were measured on 27 objects printed in three different batches (nine objects per batch). The porous fraction was computed from the following equation:

$$\text{Porous fraction } [\%] = \frac{V_{obj}[\text{m}^3] - V_{PLA}[\text{m}^3]}{V_{obj}[\text{m}^3]} \times 100 \quad (1)$$

Where:

V_{obj} represents the entire volume of the object, obtained by equation (2)

$$V_{obj}[m^3] = W[m] \times L[m] \times H[m] \quad (2)$$

V_{PLA} represents the volume occupied by PLA and is obtained by equation (3)

$$V_{PLA}[m^3] = \frac{m[kg]}{\rho_{PLA}[kg/m^3]} \quad (3)$$

Where:

m is the mass of the object;

ρ_{PLA} is the density of PLA, equal to 1250 kg/m³ [27].

These experimental values were compared to the theoretical porous fraction measured with Netfabb Basic (V5.1) on the models used for printing.

2.5. Surface topography

PVA-supported PLA structures, treated with water to remove PVA, were analyzed with a Dektak XT (Bruker, USA) profilometer equipped with a 0.7 µm diameter needle and using the Vision64 acquisition software (V5.40). As the surface at the edges of the samples was analyzed, the gyroid structure was filled almost entirely with a large cube to prevent the needle of the profilometer to be stuck in a pore (Figure 3). Three different sides of each sample (N=3) were scanned with a line resolution of 0.075 µm/pt and a 12 µm distance was applied between analyzed lines. The force applied on the needle was 0.06 mg (sides) and 0.5 mg (top).

2.6. Crystallinity fraction evaluation

PVA-supported PLA gyroid structures, treated with water to remove PVA, and PLA control samples were annealed overnight at 80°C. Crystallinity, glass transition temperature (T_g) and change in specific heat capacity (ΔC_p) at the T_g of annealed and not annealed printed samples were measured by

differential scanning calorimetry (Mettler Toledo DSC821, Belgium). Calibration was done with Indium. Samples were cut to obtain fragments with a mass ranging from 8 to 11 mg ($n=3$ per condition) and loaded into 40 μl aluminum pans. For T_g measurement and ΔC_p at this T_g , a temperature ramp was applied from 20°C to 250°C at a rate of 10°C/min. The samples were then cooled at a rate of 10°C/min, and a second cycle was used as polymer state control. For crystallinity measurement, the heating ramp was increased to 100°C/min in order to minimize sample re-crystallization inside the chamber. Percentage of crystallinity was computed based on the linear increase of enthalpy of fusion with crystallinity, and using a reference heat of enthalpy of 0 J/g and 93.1 J/g for theoretically 0% and 100% crystalline PLA, respectively.

2.7. Compression tests

Compression tests were performed (LRX plus, Lloyd Instruments, max load = 1 kN) on both amorphous and crystalline gyroids ($n=3$), control 400 μm ($n=3$) and control 100 μm ($n=3$) structures to evaluate the effect of mesh geometry, crystallinity and printing resolution on scaffold mechanical properties. The speed used for the compression test was 1 mm/min. Each sample was placed between two parallel steel plates along two axes: perpendicularly and parallel to the printed layers of the sample. Force and displacement were recorded and converted into stress and strain, respectively, taking into account scaffold dimensions. The square coming from the horizontal cross section of the imaginary cube containing the scaffold was chosen as the area needed for the conversion of force into strain. Apparent compression moduli were obtained from the slope of the linear region of the sigmoid (slope at the initial linear part of stress-strain curve) and yield strengths were extracted using the offset method with a value of 1 % (see Figure SI2 in Supporting Information for details).

2.8. Scaffold *in vitro* degradation

Amorphous ($n=4$) and annealed ($n=4$) gyroid, control 100 μm and control 400 μm structures were weighed. They were then disinfected in ethanol 70%, dried and placed in 5 ml of phosphate buffered saline (PBS) containing 0.5% of NaN_3 to avoid development of microorganisms. Samples were

incubated at 37°C and each week, half of the degradation medium was replaced by fresh PBS containing NaN₃. Each month, samples were dehydrated in ethanol and dried at 37°C during 6 h and then weighed. Only the main parts of samples (pieces bigger than 1 strut) were taken into account. Again, samples were disinfected in ethanol 70%, rinsed twice in PBS and once in PBS containing 0.5% of NaN₃ before placing them back in their own degradation medium (5 ml PBS containing 0.5% of NaN₃). The study was carried out until the main body of the scaffold fell apart. At week 64, pictures of the samples were taken with a low magnification microscope, at the same magnification (12X) and with the same backlight intensity.

2.9. Statistical analysis

ANOVA and Tukey's HSD were performed using JMP®, Version 12 Pro. (SAS Institute Inc., USA) ($\alpha=0.05$).

3. Results and discussion

3.1. 3D scanning of printed gyroid structures

The HIPS-supported gyroid structure was scanned by μ CT after HIPS dissolution. Figures 2.a and 2.b show the model and the printed gyroid scan, respectively, both cropped at the front and the top of the structure for the sake of clarity. The three-dimensional reconstruction matches the computerized model very well, and nodes as well as gyrating junctions are well defined and clearly visible. Besides, the μ CT scan shows large pores that are completely interconnected. Cross-sections can be extracted and isolated from the 3D *in silico* model and from the μ CT scan. Figure 2.d presents a printed slice of the sample, which is in close agreement with the slice coming from the model (Figure 2.c). This cross-section shows that the bean-shaped units, corresponding to the pillars of the gyroid structure, are similar to the model. Besides a good nutrient and waste diffusion, the interconnection and the large pore size (pore projections of 800 μ m) should allow a good cell-cell communication and favor tissue ingrowth. As pore projections are at least 10 times larger than cells, this structure should allow cells to migrate, proliferate and differentiate within the scaffold, and vascularization could be initiated [11]. Geometrical scaffold properties such as pore size and shape and even local curvature were shown to have an impact on the control of cell proliferation and fate, both *in vitro* and *in vivo* [38]. Depending on pore size and scaffold dimensions, a dynamic culture environment (with perfusion reactors) is sometimes needed to increase mass transport of nutrient and oxygen [39]. Flow-associated shear stress linked to geometric features of the scaffold has been shown to influence neo-tissue growth kinetics. Small shear stress (0.015 Pa for human bone marrow MSCs) has a positive effect while higher shear stresses (0.05 Pa) decrease neo-tissue growth or result in inhomogeneous tissue-engineered constructs. The spring shape design of the gyroid shows a lot of curved surfaces and only rare spots of the structure would be perpendicular to the flow in the case of culture in dynamic conditions. Shear stress should therefore be reduced compared to a strut-based scaffold, and flow patterns should be more uniform. The printed gyroid structure is thus an appropriate scaffold for tissue reconstruction.

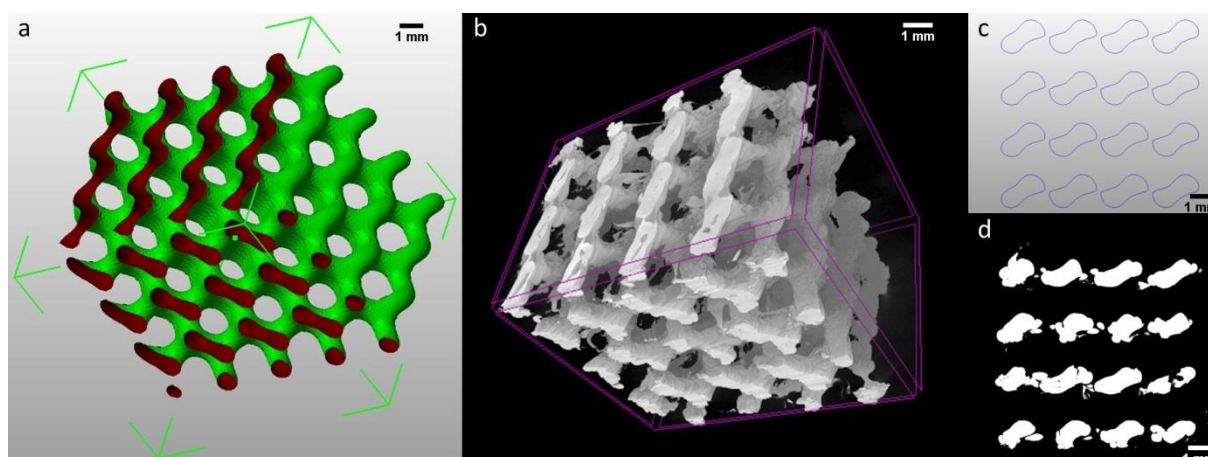


Figure 2: Model (a) and printed gyroid μ CT scan (b) both cropped at the front and the top of the structure for the sake of visualization. Model (c) and μ CT scan (d) of the corresponding printed cross-sections.

3.2. Porosity of printed gyroids

In complement to the 3D visualization of the gyroid structure, its porous fraction was determined, based on the mass and dimensions of the samples (see 2.4), and on μ CT stack images (Table 1). Both values were compared to the porosity predicted theoretically, according to the *in silico* model. In each case, porosity is in the range of 70-75%. The similarity of experimental and theoretical porosity values, as well as the small standard deviation of experimental values based on mass and dimensions emphasize the reliability of the gyroid model printing. Moreover void fraction is important as it will affect mechanical resistance.

Table 1: Printed gyroid porosity computed from mass and dimensions of gyroid structure (N=27; standard deviation; middle) and from μ CT images processing (N=1; bottom), as compared to the theoretical value (top).

	Porosity (%)
Theoretical	73.7
Experimental – From mass and dimensions	70.8 (0.5)
Experimental – From μ CT scan images	74.7

3.3. Profilometry of printed gyroid scaffolds

Characterization was further conducted at the micrometer scale, which is of interest regarding cell-material interactions. Profilometry was used to analyze the surface at the edges of the sample. As represented in Figure 3, the top and two sides of printed cubes, representing different orientations of the junctions compared to the printed layer, were analyzed. Profilometry analysis shows the stacked polymer layers of around 100 μm thick. The surface of these layers is, in each case, rather smooth at the micrometer scale. Despite the presence of the layering artifact, the 3D design is respected at the 100 μm -scale, as already evidenced by the μCT scan (N=3). Micro- and nano-topography on 2D surfaces has been shown to influence cell shape, morphology and in some cases proliferation. Cells from many different origins were shown to align parallel to micro- and nano-grooves and, in some cases, this even influenced their migration [40-42]. Here, cells could align parallel to the grooves created by the stacking of the layers. This layer artifact inherent to 3D printing techniques could be exploited to guide cell growth and migration.

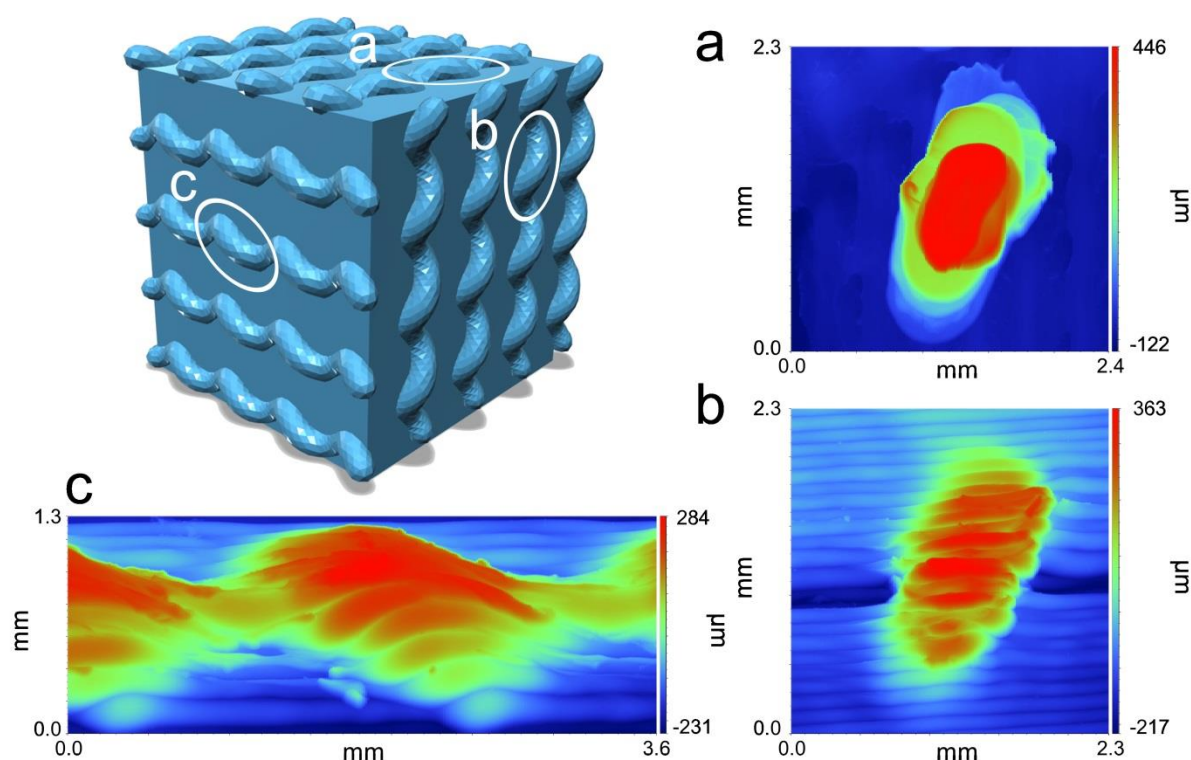


Figure 3: Simplified geometry for profilometry analysis (upper left) and topographic scans obtained by profilometry of circled areas on the top (a) and two different sides (b, c) of the sample.

3.4. Influence of the support on shape fidelity

The need of a supporting polymer to achieve good gyroid printing was investigated. Since most of the structure is self-supported, almost no overhang is present in the design, and all bridges are sufficiently small for the printer to overcome printing issues, printing without support should be possible and would constitute an interesting alternative since a dissolution step would not be required to eliminate the supporting material. Gyroids were printed with and without the addition of PVA in the second nozzle. Scaffold morphology was significantly impacted by the absence or presence of a supporting structure during printing, as it can be observed in figure 4 where black arrows point out the presence of polymer leaking out of the nozzle, known as oozing, on the non-supported samples and their absence on the supported ones. In addition, the support improves the deposition of the layers with straight orientation instead of wavy-like structure (grey arrows) and leads to less polymer drops (white arrows). The support improves the printing quality, even though the structure can be printed without support. The absence of support results in a decrease of shape accuracy.

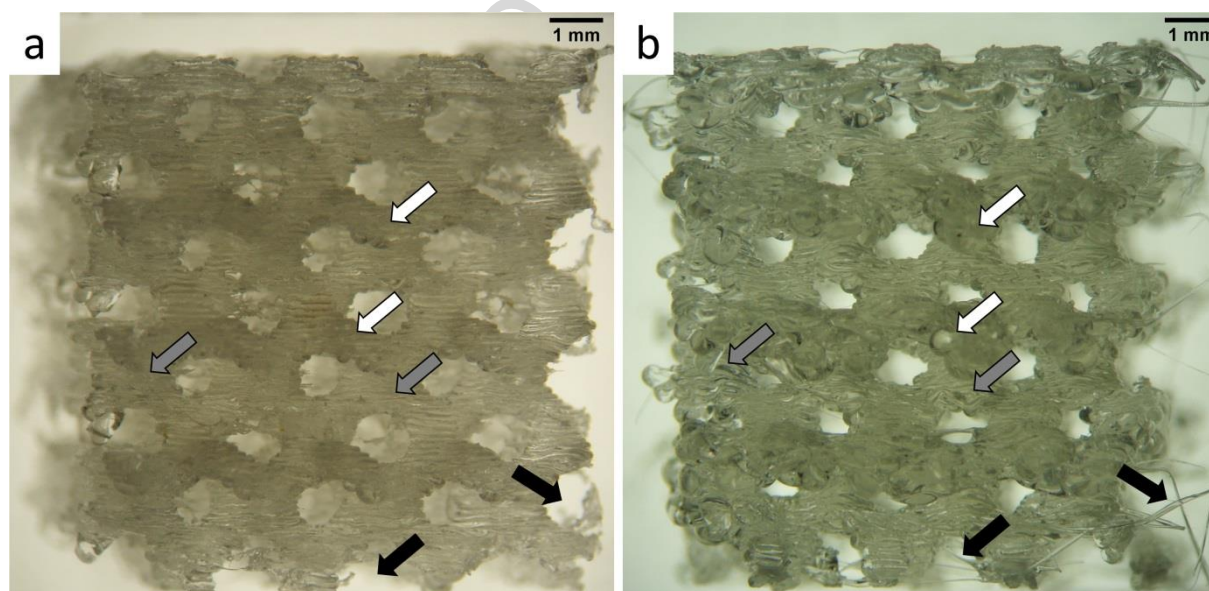


Figure 4: Pictures of gyroid structures printed with (a) and without (b) PVA support (that was later dissolved in water). Black, grey and white arrows show the presence or absence of stringing, wavy like layers and polymer drops, respectively.

3.5. Impact of annealing on printed PLA

The crystallinity of printed samples annealed overnight at 80°C was compared to the crystallinity of the as-printed polymer, using DSC (Table 2). For all samples, T_g values were close to each other and to the theoretical value of around 58°C [27]. The structures, regardless of the design, came out of the printer in an amorphous state (crystallinity below detection level). The absence of crystallinity for not-annealed samples can be easily explained by a quick cooling of the polymer once deposited by the nozzle after being melted at 220°C (melting point around 150°C). The polymer does not have time to crystallize before reaching its T_g . Sample annealing overnight at 80°C is sufficient to reach a crystallinity of 37% for the gyroid structure, and of 40% for the control structures. Upon annealing, the polymer is kept at a temperature above the T_g during a period of time sufficient for the chains to rearrange in small crystalline zones and form spherulites. These results are consistent with the measurement of ΔC_p , ie the energy required to turn the state of the amorphous part of a polymer from vitreous to viscous, which is around 0.53 J.g⁻¹.K⁻¹ for the amorphous samples compared to 0.22 J.g⁻¹.K⁻¹ for the annealed ones. This annealing process, performed after printing the structures, can be used to modify the crystallinity of the scaffold and hence, to tune its mechanical properties and its degradation rate.

Table 2: DSC measurement of glass transition temperature (T_g), change in specific heat capacity (ΔC_p) and degree of crystallinity for not-annealed and annealed gyroid and control samples. Mean (standard deviation); BDL = below detection limit (N=3).

Sample	Annealing	T_g (°C)	ΔC_p (J.g ⁻¹ .K ⁻¹)	Crystallinity (%)
Gyroid	No	59.4 (0.2)	0.55 (0.02)	BDL
	Yes	58.1 (0.2)	0.23 (0.02)	36.6 (0.9)
Control 400 µm	No	58.0 (0.5)	0.51 (0.04)	BDL
	Yes	58.0 (0.7)	0.22 (0.02)	40.2 (0.2)
Control 100 µm	No	59.2 (0.4)	0.55 (0.01)	BDL
	Yes	57.3 (0.3)	0.20 (0.02)	39.6 (0.9)

3.6. Impact of geometry, printing resolution and crystallinity of the structures on mechanical resistance

The gyroid structure was chosen for its spring shape design that should provide isotropic resistance to pressure and high elasticity. Mechanical tests were performed to study the behavior of the structure depending on (i) the direction of compression with respect to the printed layers, (ii) printing resolution, and (iii) polymer crystallinity. All these parameters are expected to influence the mechanical properties of a scaffold [43-45]. Figure 5 presents a typical stress-strain curve for each type of sample and in each direction of compression (force applied parallel or perpendicular to the printed layers). Stress-strain curves can be compared for the different conditions as the nature of the polymer and the porosity were kept the same. For the crystalline and amorphous gyroid structures, the curves are similar whatever the compression direction. In contrast, the compression direction significantly impacts the behavior of control scaffolds. When the compression load is applied parallel to the printed layers, peaks appear in the graphs. This phenomenon is due to buckling of the columns of the structures, one level after the other, in the process of compression. The crystallinity and the thickness of the printed layers do affect this buckling behavior. Yield strengths were determined (see Supporting Information, Figure S13) and they are significantly higher for crystalline samples and for thicker printed layers (400 μm versus 100 μm). This means that more pressure is needed to allow the buckling of the columns for crystalline compared to amorphous samples, as well as for thicker compared to thinner printed layers. This was expected since buckling is a phenomenon of elastic instability, which happens at lower loads when the bending stiffness of a loaded column decreases. Bending stiffness is proportional to the elastic modulus, which will be higher for the crystalline phase. On the other hand, thinner printed layers create more weak boundaries within each column, which may decrease bending stiffness.

Slopes were extracted from the linear part of the stress-strain curves, to give an apparent compression modulus (see Supporting Information, Figure S13). The results show that the gyroid structure, with an apparent compression modulus of about 50 MPa, has a more deformable behavior owing to its spring shape. Besides, layer thickness has an effect only if the load is applied parallel to

the printed layers. The crystallinity, surprisingly, does not have much influence on the apparent compression modulus.

These results reveal a clear effect of the mesh geometry, the printed layer thickness and the crystallinity on the resistance to compression. The gyroid sample shows a more deformable and isotropic behavior when compressed compared to both control structures. This isotropy is of high interest in tissue engineering as it would allow the printing and the implantation of scaffolds that would support the pressure coming from any direction equally, regardless of the printing or implant orientation.

Gyroid geometry was studied in the case of Solid Freeform Fabrication of metals (titanium alloys). Even though materials are different than in the present study, comparison between structure geometries can be discussed [46]. Changing the eccentricity of pore projections in a gyroid design influenced elastic moduli and compressive strength [33]. Mechanical properties of titanium alloy gyroids were compared to octahedron models and displayed a higher yield and plateau stress [47]. A superior fatigue resistance was also evidenced and could be attributed to the continuous rate of curvature of gyroids, removing nodal points which may favors cracks initiation. However, all these compression studies were realized along only one axis. As shown by Heintz *et al.*, loads applied in other directions can strongly modify the mechanical behavior of the structure [43]. They compared a gyroid and a strut-based design printed in titanium alloy. Both gyroid and strut-based structure showed an elastic modulus 2 and 3 times lower, respectively, for a compression parallel to printed layers if compared with a perpendicular compression. This is, however, quite inconsistent with our results, as in our case the lower moduli were observed for a compression perpendicular to printed layers. This could be due to the difference in the model used (size of struts, space between strut, etc) or to the difference in product manufacture (electron beam melting versus fused deposition modeling).

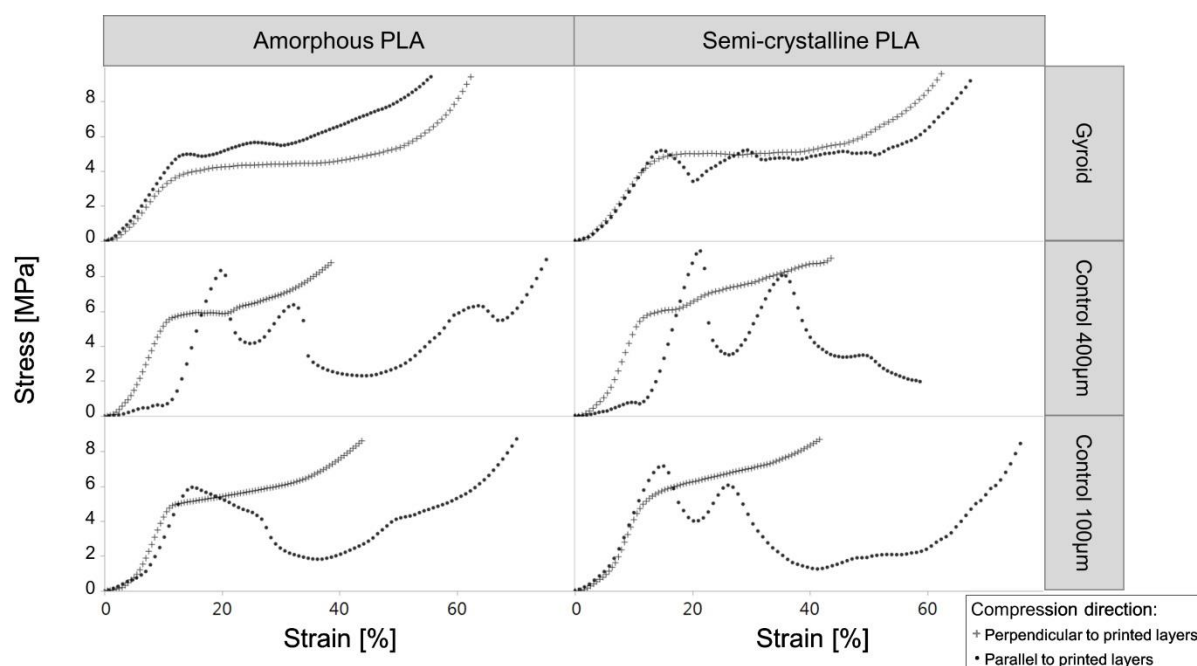


Figure 5: Stress-strain curves of amorphous (left) and semi-crystalline (right) gyroid (top) and control samples (middle and bottom) along two axes: perpendicular (+) and parallel (•) to printed layers. Results were obtained in triplicate but a single representative result is shown for the sake of clarity. All curves are available in Supporting Information (Figure S11)

3.7. Impact of geometry, printing resolution and crystallinity of the structures on *in vitro* degradation kinetics

PLA mainly degrades by ester linkage hydrolysis, which occurs in presence of water and is catalyzed in acidic or basic conditions. Gyroid and control samples, in amorphous and semi-crystalline state, were immersed in phosphate buffered saline (PBS) during 84 weeks.

The mass of the samples was stable during about 50 weeks (Figure 6). From week 52, samples started to drastically degrade. The semi-crystalline control 100 μm , amorphous gyroid and amorphous control 100 μm were the most degraded at week 84, with a remaining mass of 20, 43 and 46 % of the initial mass, respectively. The relative masses after 84 weeks were significantly higher for the 400 μm resolution samples (80 % for amorphous and 73 % for crystalline samples), meaning that thicker printed layers slow down the degradation process. Concerning the crystallinity, the effect seems less

obvious. Indeed, annealing seems to weaken 400 μm and 100 μm control samples, but not the gyroid samples.

This sudden degradation is well known for PLA and described in literature. As water is able to penetrate the PLA bulk, hydrolysis happens throughout the entire polymer matrix. This phenomenon is called “bulk degradation” and it has to be distinguished from “surface erosion” which happens in more hydrophobic polymers such as polycaprolactone. The bulk degradation of PLA is also the result of an autocatalytic process. When an ester bond is cleaved, a new carboxylic acid function is generated, the pH in the bulk decreases, and the degradation kinetic increases [27, 48].

Felfel *et al.* and Serra *et al.* did not observe significant degradation of PLA films after 8 weeks at 37°C in PBS and simulated body fluid, respectively [24, 49]. Höglund *et al.* obtained a 75 % relative mass for polylactide 3051D (NatureWorks LLC, USA) and 85 % for 250 μm -thick PLLA films after 26 weeks of degradation at 37°C in PBS [50]. Ravi *et al.* worked on 3D printed porous sheets (800 μm thick) and measured relative masses between 76 and 89 % after 26 weeks for the same polymer (PLLA, PURAC, The Netherlands) for distinct pore designs [51]. Both studies showed higher degradation rates compared to our study. However, both PLA source and sample geometry/dimensions were different. Indeed, several factors influence PLA degradation rate including the morphology, degree of crystallinity, molar mass, hydrophobicity, size and geometry of the samples, stereocomplex formation (i.e. formation of intermolecular complexes occurring due to non-covalent bonds between enantiomeric chains), and environmental conditions (pH and temperature) [50]. In some cases, the complete degradation of PLA can take more than 3 years [49]. These differences in degradation time emphasize the importance of extended degradation studies on real or close-to-real sample sizes and geometries.

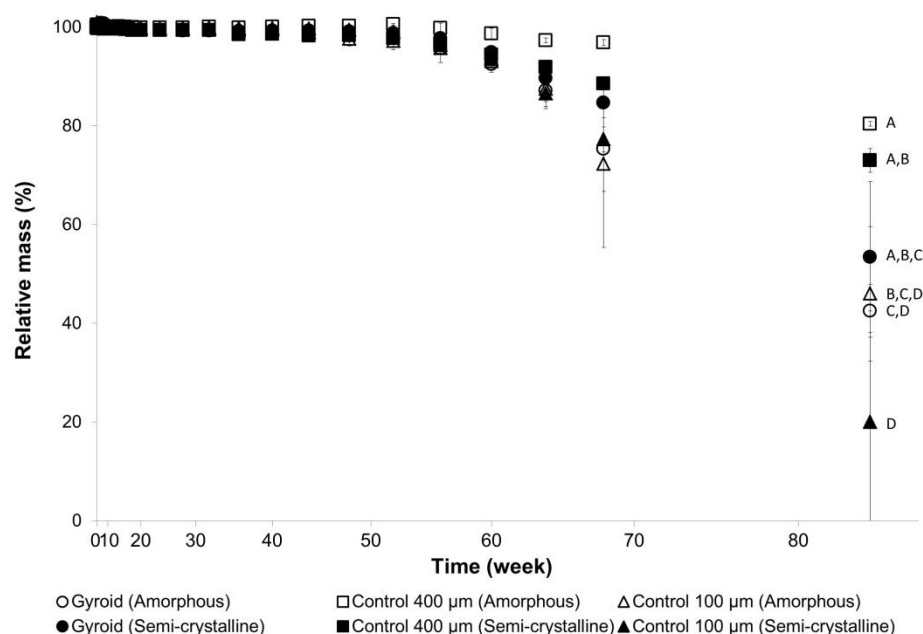


Figure 6: Degradation of not-annealed and annealed gyroid and control samples in phosphate buffered saline (PBS). For the sake of clarity, a non-linear x axis was used (the square of the number of weeks was used to build the scale) (error bar= standard deviation, N=4). Values not sharing the same letter are significantly different ($\alpha=0.05$).

Photographs of the degraded structures were taken at week 64 (Figure 7) and macroscopic changes are visible for amorphous scaffolds: a change in color, from clear and translucent to a milky white and completely opaque polymer. Although sample masses were stable for 50 weeks, this observation was already visible after 3 weeks. This has already been attributed to the swelling of PLA at an early stage of the bulk erosion process [51] which leads to a change in optical properties. In contrast, such change was not observed for crystalline samples, which were less translucent initially.

Scaffold geometry also impacts degradation. Control scaffolds degrade by losing struts one after the other, whereas the gyroid structure tends to retain its integrity. This could be related to the inclination angles of the circular gyroid struts that continuously vary all over the structure. This results in slight changes in area and position between two adjacent layers [31]. The layers are then more interconnected in the case of the gyroid compared to the strut-based scaffold, which has only a few connection points between struts of different levels. However, in the case of the amorphous gyroid, cracks arise at the junctions of printed layers, resulting in elongation of the sample. Therefore, the

annealing process seems to have a positive effect on the cohesion of the printed layers of the gyroid samples.

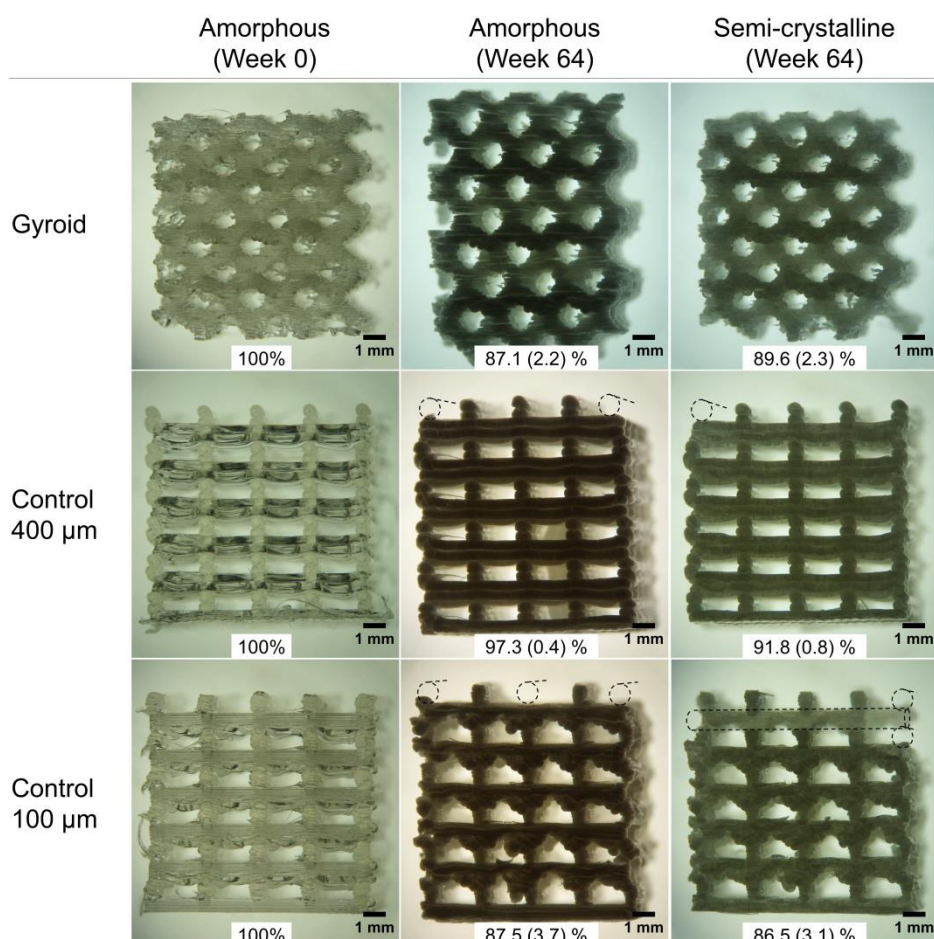


Figure 7: Pictures of gyroid (top) and control (middle – 400 μ m and bottom – 100 μ m) samples, as produced (left) or after 64 weeks of degradation (middle – amorphous samples, right – semi-crystalline samples). Dotted lines represent struts present at the beginning of the experiment that were lost due to structure degradation. Means of relative masses and standard deviations ($n=4$) are presented in white boxes.

The degradation seems affected only by printed layer thickness, a higher thickness reducing the speed of the process. Neither crystallinity nor mesh geometry affects significantly the degradation rate even though the change in mesh geometry will influence the detachment of pieces from the structures. Besides this, the annealing process improves layers attachment in the case of gyroid samples.

4. Conclusions

A complex gyroid scaffold was printed in PLA close to the resolution limit of fused deposition modeling, a simple and low-cost additive manufacturing technique. This geometry is particularly suitable for tissue engineering approaches given the large pore size, high porous volume and mechanical robustness. The reliability of the printing procedure was demonstrated based on a μ CT scan, on porous volume measurement and on surface topography analysis. PLA is a FDA-approved biodegradable and implantable polymer. The water-soluble PVA support was shown to be important to obtain a controlled and well-defined shape of the gyroid structure, and it can be easily dissolved after printing. Annealing was used to increase the crystallinity fraction of the polymer, with a view to tune mechanical properties and degradation rate. Mechanical compression tests showed that crystallinity, layer resolution, and especially the structure design influence the stress-strain curves. Moreover, the gyroid structure presents an isotropic behavior regarding compression, in contrast with strut-based designs commonly reported in the literature. Degradation tests highlighted the faster degradation for thinner printed layers, whereas the gyroid geometry prevents the detachment of pieces from the structure upon degradation, and the annealing process increases layers attachment. Results, brought together, show that the gyroid design shows superior properties to be used for personalized implantable scaffolds for tissue engineering.

5. Acknowledgements

We sincerely thank Michel Sclavons and Prof. Sophie Demoustier-Champagne for helpful discussions, the Bio- and Soft Matter division (BSMA) for access to the 3D printer, Julian Leprince for access to the mechanical test instrument and Luc Randolph for his help in stress-strain curve analysis, Pascal Van Velthem for DSC training, Prof. Arnaud Delcorte for access to the profilometer and Claude Poleunis for the training, and Prof. Yves Dufrêne for access to the low magnification microscope. The work was supported by the Interuniversity Attraction Pole Program (P07/05) and the Belgian National Foundation for Scientific Research (FNRS). Anne des Rieux is a F.R.S.-FNRS Research Associate.

6. Data availability

The raw/processed data required to reproduce these findings cannot be shared at this time due to technical or time limitations.

7. References

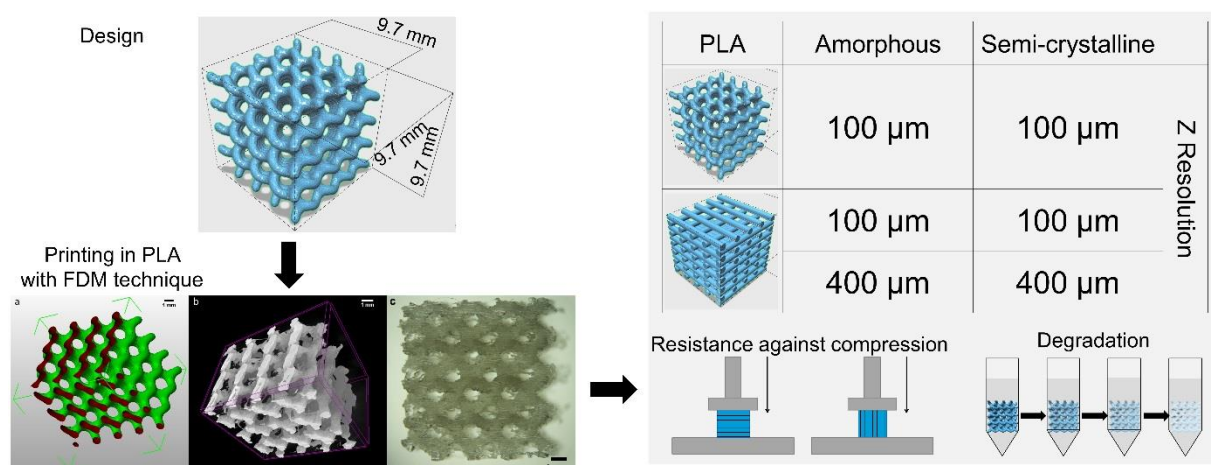
- [1] M. Verhulsel, M. Vignes, S. Descroix, L. Malaquin, D.M. Vignjevic, J.L. Viovy, A review of microfabrication and hydrogel engineering for micro-organs on chips, *Biomaterials* 35(6) (2014) 1816-1832.
- [2] S.C. Cox, J.A. Thornby, G.J. Gibbons, M.A. Williams, K.K. Mallick, 3D printing of porous hydroxyapatite scaffolds intended for use in bone tissue engineering applications, *Mat Sci Eng C-Mater* 47 (2015) 237-247.
- [3] E.T. Pineda, R.M. Nerem, T. Ahsan, Differentiation patterns of embryonic stem cells in two- versus three-dimensional culture, *Cells Tissues Organs* 197(5) (2013) 399-410.
- [4] L. Tang, X. Lu, R. Zhu, T. Qian, Y. Tao, K. Li, J. Zheng, P. Zhao, S. Li, X. Wang, L. Li, Adipose-Derived Stem Cells Expressing the Neurogenin-2 Promote Functional Recovery After Spinal Cord Injury in Rat, *Cell Mol Neurobiol* 36(5) (2016) 657-667.
- [5] F. Gao, S.M. Chiu, D.A.L. Motan, Z. Zhang, L. Chen, H.L. Ji, H.F. Tse, Q.L. Fu, Q. Lian, Mesenchymal stem cells and immunomodulation: current status and future prospects, *Cell Death Dis* 7 (2016) e2062.
- [6] S. Park, G. Kim, Y.C. Jeon, Y. Koh, W. Kim, 3D polycaprolactone scaffolds with controlled pore structure using a rapid prototyping system, *J Mater Sci-Mater M* 20(1) (2009) 229-234.
- [7] T.A.E. Ahmed, E.V. Dare, M. Hincke, Fibrin: A versatile scaffold for tissue engineering applications, *Tissue Eng Pt B-Rev* 14(2) (2008) 199-215.
- [8] H. Lee, S. Ahn, L.J. Bonassar, G. Kim, Cell(MC3T3-E1)-printed poly(ϵ -caprolactone)/alginate hybrid scaffolds for tissue regeneration, *Macromol Rapid Comm* 34(2) (2013) 142-149.
- [9] J.W. Jung, J.H. Park, J.M. Hong, H.-W. Kang, D.-W. Cho, Octahedron pore architecture to enhance flexibility of nasal implant-shaped scaffold for rhinoplasty, *Int J Precis Eng Man* 15(12) (2014) 2611-2616.
- [10] J.E. Trachtenberg, P.M. Mountziaris, J.S. Miller, M. Wettergreen, F.K. Kasper, A.G. Mikos, Open-source three-dimensional printing of biodegradable polymer scaffolds for tissue engineering, *J Biomed Mater Res A* 102(12) (2014) 4326-4335.
- [11] H. Seyednejad, D. Gawlitta, R.V. Kuiper, A. de Bruin, C.F. van Nostrum, T. Vermonden, W.J.A. Dhert, W.E. Hennink, In vivo biocompatibility and biodegradation of 3D-printed porous scaffolds based on a hydroxyl-functionalized poly(ϵ -caprolactone), *Biomaterials* 33(17) (2012) 4309-4318.
- [12] B.C. Gross, J.L. Erkal, S.Y. Lockwood, C. Chen, D.M. Spence, Evaluation of 3D printing and its potential impact on biotechnology and the chemical sciences, *Anal Chem* 86(7) (2014) 3240-3253.
- [13] G. Thrivikraman, A. Athirasala, C. Twohig, S.K. Boda, L.E. Bertassoni, Biomaterials for Craniofacial Bone Regeneration, *Dent Clin N Am* 61(4) (2017) 835-856.
- [14] L. Ho, S.-h. Hsu, Cell reprogramming by 3D bioprinting of human fibroblasts in polyurethane hydrogel for fabrication of neural-like constructs, *Acta Biomater* 70 (2018) 57-70.
- [15] M.D. Giuseppe, N. Law, B. Webb, R. A. Macrae, L.J. Liew, T.B. Sercombe, R.J. Dilley, B.J. Doyle, Mechanical behaviour of alginate-gelatin hydrogels for 3D bioprinting, *J Mech Behav Biomed* 79 (2018) 150-157.
- [16] J.M. Walker, E. Bodamer, O. Krebs, Y. Luo, A. Kleinfehn, M.L. Becker, D. Dean, Effect of Chemical and Physical Properties on the In Vitro Degradation of 3D Printed High Resolution Poly(propylene fumarate) Scaffolds, *Biomacromolecules* 18(4) (2017) 1419-1425.

- [17] B.N. Teixeira, P. Aprile, R.H. Mendonça, D.J. Kelly, R.M.d.S.M. Thiré, Evaluation of bone marrow stem cell response to PLA scaffolds manufactured by 3D printing and coated with polydopamine and type I collagen, *J Biomed Mater Res B* 0(0) (2018) 000-000.
- [18] A. Barba, A. Diez-Escudero, Y. Maazouz, K. Rappe, M. Espanol, E.B. Montufar, M. Bonany, J.M. Sadowska, J. Guillem-Marti, C. Öhman-Mägi, C. Persson, M.-C. Manzanares, J. Franch, M.-P. Ginebra, Osteoinduction by Foamed and 3D-Printed Calcium Phosphate Scaffolds: Effect of Nanostructure and Pore Architecture, *ACS Appl Mater Inter* 9(48) (2017) 41722-41736.
- [19] C. Deng, Q. Yao, C. Feng, J. Li, L. Wang, G. Cheng, M. Shi, L. Chen, J. Chang, C. Wu, 3D Printing of Bilineage Constructive Biomaterials for Bone and Cartilage Regeneration, *Adv Funct Mater* 27(36) (2017) 1703117.
- [20] J.A. Kim, H.-s. Yun, Y.-A. Choi, J.-E. Kim, S.-Y. Choi, T.-G. Kwon, Y.K. Kim, T.-Y. Kwon, M.A. Bae, N.J. Kim, Y.C. Bae, H.-I. Shin, E.K. Park, Magnesium phosphate ceramics incorporating a novel indene compound promote osteoblast differentiation in vitro and bone regeneration in vivo, *Biomaterials* 157 (2018) 51-61.
- [21] F. Gao, Z. Xu, Q. Liang, B. Liu, H. Li, Y. Wu, Y. Zhang, Z. Lin, M. Wu, C. Ruan, W. Liu, Direct 3D Printing of High Strength Biohybrid Gradient Hydrogel Scaffolds for Efficient Repair of Osteochondral Defect, *Adv Funct Mater* 28 (2018) 1706644.
- [22] F. Pati, D.-H. Ha, J. Jang, H.H. Han, J.-W. Rhie, D.-W. Cho, Biomimetic 3D tissue printing for soft tissue regeneration, *Biomaterials* 62 (2015) 164-175.
- [23] S. Buyuksungur, T. Endogan Tanir, A. Buyuksungur, E.I. Bektas, G. Torun Kose, D. Yucel, T. Beyzadeoglu, E. Cetinkaya, C. Yenigun, E. Tonuk, V. Hasirci, N. Hasirci, 3D printed poly(ϵ -caprolactone) scaffolds modified with hydroxyapatite and poly(propylene fumarate) and their effects on the healing of rabbit femur defects, *Biomater Sci* 5(10) (2017) 2144-2158.
- [24] T. Serra, M. Ortiz-Hernandez, E. Engel, J.A. Planell, M. Navarro, Relevance of PEG in PLA-based blends for tissue engineering 3D-printed scaffolds, *Mat Sci Eng C-Mater* 38 (2014) 55-62.
- [25] T. Serra, J.A. Planell, M. Navarro, High-resolution PLA-based composite scaffolds via 3-D printing technology, *Acta Biomater* 9(3) (2013) 5521-5530.
- [26] A.P. Uzel, E. Seris, S. Henri, G. Jouan, P. Borget, G. Daculsi, Preclinical and clinical cases of new absorbable composite interference screws in osteoarticular surgery, *Key Eng Mater* 529-530 (2013) 325-330.
- [27] D.E. Henton, P. Gruber, J. Lunt, J. Randall, Polylactic Acid Technology, in: T.F. Group (Ed.), *Natural Fibers, Biopolymers, and Biocomposites*, CRC Press Boca Raton, 2005, pp. 527-577.
- [28] J.P. Temple, D.L. Hutton, B.P. Hung, P.Y. Huri, C.A. Cook, R. Kondragunta, X. Jia, W.L. Grayson, Engineering anatomically shaped vascularized bone grafts with hASCs and 3D-printed PCL scaffolds, *J Biomed Mater Res A* 102(12) (2014) 4317-4325.
- [29] F. Wang, L. Shor, B. Starly, A. Darling, S. Güçeri, W. Sun, Fabrication of cellular poly- ϵ -caprolactone (PCL) scaffolds by precision extruding deposition process, *Bioengineering, Proceedings of the Northeast Conference*, New Jersey, 2003, pp. 181-182.
- [30] J.A. Dolan, B.D. Wilts, S. Vignolini, J.J. Baumberg, U. Steiner, T.D. Wilkinson, Optical Properties of Gyroid Structured Materials: From Photonic Crystals to Metamaterials, *Adv Opt Mater* 3(1) (2015) 12-32.
- [31] C. Yan, L. Hao, A. Hussein, D. Raymont, Evaluations of cellular lattice structures manufactured using selective laser melting, *Int J Mach Tool Manu* 62 (2012) 32-38.
- [32] J.G. Torres-Rendon, T. Femmer, L. De Laporte, T. Tigges, K. Rahimi, F. Gremse, S. Zafarnia, W. Lederle, S. Ifuku, M. Wessling, J.G. Hardy, A. Walther, Bioactive gyroid scaffolds formed by sacrificial templating of nanocellulose and nanochitin hydrogels as instructive platforms for biomimetic tissue engineering, *Adv Mater* 27(19) (2015) 2989-2995.
- [33] A. Yáñez, A. Herrera, O. Martel, D. Monopoli, H. Afonso, Compressive behaviour of gyroid lattice structures for human cancellous bone implant applications, *Mat Sci Eng C-Mater* 68 (2016) 445-448.
- [34] Q. Wang, L. Ren, X. Li, S. Zhang, T.B. Sercombe, K. Yang, Antimicrobial Cu-bearing stainless steel scaffolds, *Mat Sci Eng C-Mater* 68 (2016) 519-522.

- [35] Y. Luo, C.K. Dolder, J.M. Walker, R. Mishra, D. Dean, M.L. Becker, Synthesis and Biological Evaluation of Well-Defined Poly(propylene fumarate) Oligomers and Their Use in 3D Printed Scaffolds, *Biomacromolecules* 17(2) (2016) 690-697.
- [36] S.C. Mauck, S. Wang, W. Ding, B.J. Rohde, C.K. Fortune, G. Yang, S.-K. Ahn, M.L. Robertson, Biorenewable Tough Blends of Polylactide and Acrylated Epoxidized Soybean Oil Compatibilized by a Polylactide Star Polymer, *Macromolecules* 49(5) (2016) 1605-1615.
- [37] C.A. Schneider, W.S. Rasband, K.W. Eliceiri, NIH Image to ImageJ: 25 years of image analysis, *Nat Methods* 9(7) (2012) 671-675.
- [38] Y. Guyot, I. Papantoniou, Y.C. Chai, S. Van Bael, J. Schrooten, L. Geris, A computational model for cell/ECM growth on 3D surfaces using the level set method: a bone tissue engineering case study, *Biomech Model Mechan* 13(6) (2014) 1361-1371.
- [39] Y. Guyot, I. Papantoniou, F.P. Luyten, L. Geris, Coupling curvature-dependent and shear stress-stimulated neotissue growth in dynamic bioreactor cultures: a 3D computational model of a complete scaffold, *Biomech Model Mechan* 15(1) (2016) 169-180.
- [40] I.A. Janson, A.J. Putnam, Extracellular matrix elasticity and topography: Material-based cues that affect cell function via conserved mechanisms, *J Biomed Mater Res A* 103(3) (2015) 1246-1258.
- [41] M.J. Dalby, M.O. Riehle, S.J. Yarwood, C.D.W. Wilkinson, A.S.G. Curtis, Nucleus alignment and cell signaling in fibroblasts: response to a micro-grooved topography, *Exp Cell Res* 284(2) (2003) 274-282.
- [42] J.L. Charest, A.J. García, W.P. King, Myoblast alignment and differentiation on cell culture substrates with microscale topography and model chemistries, *Biomaterials* 28(13) (2007) 2202-2210.
- [43] P. Heinl, L. Müller, C. Körner, R.F. Singer, F.A. Müller, Cellular Ti-6Al-4V structures with interconnected macro porosity for bone implants fabricated by selective electron beam melting, *Acta Biomater* 4(5) (2008) 1536-1544.
- [44] V. Guarino, M. Marrese, L. Ambrosio, Chemical and Physical Properties of Polymers for Biomedical Use, in: F. Puoci (Ed.), *Advanced Polymers in Medicine*, Springer International Publishing, Cham, 2015, pp. 67-90.
- [45] W. Wu, P. Geng, G. Li, D. Zhao, H. Zhang, J. Zhao, Influence of Layer Thickness and Raster Angle on the Mechanical Properties of 3D-Printed PEEK and a Comparative Mechanical Study between PEEK and ABS, *Materials* 8(9) (2015) 5834-5846.
- [46] G. Pia, M. Brun, F. Aymerich, F. Delogu, Gyroidal structures as approximants to nanoporous metal foams: clues from mechanical properties, *J Mater Sci* 52(2) (2017) 1106-1122.
- [47] M. Speirs, B. Van Hooreweder, J. Van Humbeeck, J.P. Kruth, Fatigue behaviour of NiTi shape memory alloy scaffolds produced by SLM, a unit cell design comparison, *J Mech Behav Biomed* 70 (2017) 53-59.
- [48] M.A. Woodruff, D.W. Hutmacher, The return of a forgotten polymer - Polycaprolactone in the 21st century, *Prog Polym Sci* 35(10) (2010) 1217-1256.
- [49] R.M. Felfel, K.M.Z. Hossain, A.J. Parsons, C.D. Rudd, I. Ahmed, Accelerated in vitro degradation properties of polylactic acid/phosphate glass fibre composites, *J Mater Sci* 50(11) (2015) 3942-3955.
- [50] A. Höglund, K. Odellius, A.-C. Albertsson, Crucial Differences in the Hydrolytic Degradation between Industrial Polylactide and Laboratory-Scale Poly(L-lactide), *ACS Appl Mater Inter* 4(5) (2012) 2788-2793.
- [51] P. Ravi, P.S. Shiakolas, T.R. Welch, Poly-L-lactic acid: Pellets to fiber to fused filament fabricated scaffolds, and scaffold weight loss study, *Addit Manuf* 16 (2017) 167-176.

8. Internet reference

1. <http://www.3dvia.com/content/DCA841D2E4F6C8DA> (attached licence:
<http://creativecommons.org/licenses/by-nc/2.5/>) (last view July 2016)



Graphical abstract

Highlights

- Fused deposition modeling was pushed to its resolution limit to print small poly(lactic acid) gyroid scaffolds.
- Printed gyroid structures matched the computerized model very well, and nodes as well as gyrating junctions were well defined.
- These gyroid structures were compared to commonly used strut-based structures.
- Gyroid scaffolds show an isotropic behavior regarding stress-strain curves while strut-based scaffolds exhibit an orientation-dependent deformation.
- Gyroid scaffolds retain their integrity longer in phosphate buffered saline, while common scaffolds lose struts one after another.